Particuology xxx (2020) xxx–xxx

Contents lists available at ScienceDirect

Particuology

journal homepage: www.elsevier.com/locate/partic

Production of metallic iron nanoparticles in a baffled stirred tank reactor: Optimization via computational fluid dynamics simulation

Giorgio Vilardi*, Nicola Verdone

Sapienza University of Rome, Department of Chemical Engineering Materials Environment, Via Eudossiana 18, 00184, Rome, Italy

ARTICLE INFO

Article history:
Received 11 May 2019
Received in revised form 9 July 2019
Accepted 6 December 2019
Available online xxx

Keywords:
Nano zero-valent iron
Computational fluid dynamics
Turbulence
Micromixing
Length scale

ABSTRACT

The aim of this work is to optimize iron nanoparticle production in stirred tank reactors equipped with two classical impellers: Rushton and four-pitched blade turbines, which are largely used in batch industrial synthesis and efficient scale-up. The main operative parameters of nanoparticle synthesis are the precursor initial concentration, reducing agent/precursor molar ratio, impeller–tank clearance, and impeller rotational velocity. These parameters were varied during the synthesis to find the optimal operating values based on the Fe(0) (%) production, zeta potential, particle size distribution, and powder X-ray diffraction pattern obtained. We found that the optimal operating conditions for nanoparticle production were an impeller velocity of 1500 rpm, initial iron precursor concentration of 20 mM, molar ratio of reducing agent to iron precursor of 3 mol/mol, and impeller clearance of 0.25 and 0.4 times the vessel diameter for Rushton and four-pitched blade impellers, respectively. Setting these conditions achieved a total conversion of 0.94–0.98 and yielded a product with a unimodal size distribution and average diameters in the range 30–50 nm. The computational fluid dynamics results agreed with the expectations, and the obtained mixing Damkohler numbers show that the process is mixed controlled.

Introduction

Nanoparticles have been widely synthesized in the last two decades because of their technological applications (Afify & Elgazery, 2016; Li, Hu, Huang, & Li, 2013; Mohammed, Gomaa, Ragab, & Zhu, 2017; Surinwong & Rujiwatra, 2013; Xu, 2008). Many researchers have focused mainly on producing monodisperse nanoparticles with controlled particle sizes (Di Palma, Gueye, & Petrucci, 2015), because their special optical, electrical, chemical, and magnetic characteristics depend strongly on their size and structure (quantum size effect (Halperin, 1986)). In particular, iron metallic nanoparticles in the form of nano zero-valent iron (nZVI) have received interest owing to their various industrial (Vispute, Zhang, Sanna, Xiao, & Huber, 2010) and environmental applications (Mata, Bhaskaran, & Sadras, 2016), which have led to impressive results compared with those obtained by conventional technologies. Iron nanoparticles can be synthesized through both bottom-up and top-down approaches. The former are usually based on thermal decomposition of the metastable organometallic compound iron pentacarbonyl, which can yield nanoparticles with mean size <10 nm (Farrell, Majetich, & Wilcoxon, 2003; Huber, 2005). However, the most diffuse synthesis of nZVI is wet-chemical synthesis based on reduction of ferrous or ferric ions in an aqueous or organic/aqueous medium through a reducing agent (sodium/lithium borohydride, hydrazine (Huber, 2005; Li et al., 2006; Shi, Lin, Zhang, & Chen, 2011; Singh, Misra, & Singh, 2011)). Surfactants and dispersed agents such as carboxy-methylcellulose (He & Zhao, 2007), xanthan gum (Xin, Tang, Zheng, Shao, & Kolditz, 2016), and other bio-polymers (Wang et al., 2017) are usually used to prevent or limit agglomeration of produced insoluble metal nanoparticles.

The three main challenges for producing a nano-product of good quality are: (i) controlling the particle size, (ii) achieving monodispersity, and (iii) minimizing the amount of oxidation. Micromixing conditions must be achieved to produce nano-sized particles in a classical stirred tank reactor (Gavi, Marchisio, & Barresi, 2008). Micromixing is molecular-scale mixing and, considering the very high reaction rates of nanoparticle synthesis, greatly affects the particle size distribution (PSD) of the products (Pohl, Jamshidi, Brenner, & Peuker, 2012). Mixing determines the

Abbreviations: CFD, computational fluid dynamics; CMC, carboxy-methylcellulose; FPB, four-pitched blade; nZVI, nano zero-valent iron; PDE, partial differential equation; PSD, particle size distribution; RANS, Reynolds-averaged Navier–Stokes; RT, Rushton turbine; XRD, X-ray diffraction.

* Corresponding author.
E-mail address: giorgio.vilardi@uniroma1.it (G. Vilardi).

https://doi.org/10.1016/j.partic.2019.12.005

Please cite this article in press as: Vilardi, G., & Verdone, N. Production of metallic iron nanoparticles in a baffled stirred tank reactor: Optimization via computational fluid dynamics simulation. *Particuology* (2020), https://doi.org/10.1016/j.partic.2019.12.005

Nomenclature

η	Kolmogorov scale, m
ε	Turbulent kinetic energy dissipation rate, m^2/s^3 or W/kg
ν	Kinematic viscosity, m^2/s
Re	Impeller Reynolds number
λ_b	Batchelor scale, m
Sc	Schmidt number
D	Molecular diffusion coefficient, m^2/s
D_i	Impeller diameter, m
T	Tank diameter, m
C	Impeller clearance, m
H	Liquid hold-up, m
N	Impeller rotational velocity, rps or rpm
C_0	Fe(II) initial concentration, M or mM
u	Velocity field, m/s
p	Pressure, Pa
ν_T	Turbulent eddy viscosity, m^2/s
k	Turbulent kinetic energy, J/kg or m^2/s^2
C_μ, C_1, C_2, σ_k, σ_ε	Empirical constants of k–ε model
N_p	Impeller power number
ρ_L	Liquid density, kg/m^3
r [m], *z* [m], θ [rad]	Cylindrical coordinates
V_T	Tank diameter, m^3
P	Power required to drive the impeller, W
γ	Impeller torque, Nm
ε_g	Turbulent kinetic energy dissipation rate with respect to the tank, m^2/s^3 or W/kg
Fr	Froude number
g	Acceleration of gravity, m/s^2
τ_b	Blending time according to Grenville theory, s
τ_m	Generic characteristic mixing time, s
τ_k	Kolmogorov mixing time, s
τ_{bc}	Batchelor mixing time, s
τ_c	Corrsin mixing time, s
τ_E	Engulfment mixing time, s
τ_r	Characteristic reaction time, s
Da_m	Mixing Damkohler number
k_{obs}	Observed kinetic constant, $m^{3(n-1)}/mol^{n-1}$ s or L^{n-1}/mol^{n-1} s
n	Reaction kinetic order
Q_r	Inlet flowrate of reducing agent solution, mL/min
Q_{in}	Total inlet flowrate, m^3/s
Q_{out}	Total outlet flowrate, m^3/s
r	Reaction rate, mol/m^3 s
t	Time, s
c	Specific chemical species concentration, mol/m^3
Q	Flowrate, m^3/s

build-up of supersaturation, on which the nucleation and molecular growth rate depend. Considering that a slight supersaturation increase can cause an increase in nucleation rate of several orders of magnitude but a limited increase in nuclear growth rate (crystal growth), it is obvious that nucleation dominates over growth at high supersaturation levels, and small particles are produced (Wang & Fox, 2004). Indeed, particles can also grow by aggregation and through collision and adhesion depending on the collision frequency and aggregation efficiency of the specific process. Therefore, achieving suitable product size and quality requires mixing time scales on the same order of magnitude (or lower) as the extremely high nucleation and growth rates of nanoparticle synthesis in wet reduction. An increase in micro-mixing intensity leads to a remarkable increase in the interfacial area available for diffusion, implying enhanced molecular contact. This means that molecular segregation is dramatically reduced on the micromixing scale.

Eddy diffusion or turbulent diffusion can occur on the Kolmogorov scale η (m) given by $\eta = (\nu^3/\varepsilon)^{1/4}$, where ε (m^2/s^3 or W/kg) is the turbulent kinetic energy dissipation rate and ν (m^2/s) the kinematic viscosity. Eddies are groups of molecules that cause mass transfer on the molecular scale through their motion. According to the Richardson energy cascade theory (Pope, 2000; Richardson, 1922), turbulent flow can be divided into (i) eddies of equal length scales and (ii) the rotational velocity of the system (integral length scale). These eddies are not stable owing to the transported kinetic energy and tend to break up gradually into smaller eddies with lower rotational velocity, transferring kinetic energy until the eddy Reynolds number *Re* is low enough for stable motion. The molecular viscosity of the eddies effectively dissipates kinetic energy. Therefore, the Kolmogorov scale represents the minor eddy size in the system. The greater the energy dissipated on the Kolmogorov scale is, the more homogeneous the molecular scale is, improving the contact among the reacting molecules. Turbulence alone cannot provide the degree of mixing required for fast reactions; thus turbulent diffusion plays an important role.

Another fundamental scale in reactive mixing is the Batchelor scale λ_b (m) given by $\lambda_b = \eta/Sc^{1/2}$, where $Sc = \nu/D$ is the Schmidt number and D (m^2/s) is the molecular diffusion of a specific species in the solvent or the binary molecular diffusion. This scale represents "the size of a pure sphere of dye that will diffuse in exactly the time it takes the energy in an eddy of size η to dissipate" (Batchelor, 1959). For liquids, $Sc > 1$ and $\eta > \lambda_b$; thus mixing is slowed down by molecular diffusion. The Batchelor scale is ultimately the one needed for the reaction and is about equal to the molecular size (particularly for a low-viscosity liquid). The mixing efficiency also strongly depends on mixing tool characteristics such as impeller type and dimension with respect to the tank diameter, and thus on the hydrodynamic field established in agitated vessels.

In this work, nZVI particles were produced via borohydride reduction using carboxy-methyl-cellulose (CMC) as a dispersing agent in a baffled laboratory-scale stirred tank reactor, alternately equipped with a radial-impeller Rushton turbine (RT) and a mixed-flow four-pitched blade (FPB) turbine. We analyzed the effect of different operative conditions (impeller rotational velocity, impeller clearance, BH_4–/Fe(II) molar ratio, and initial ferrous ion concentration) on Fe(0) (%) production and PSD. The hydrodynamic fields in the reactor were simulated and analyzed via computational fluid dynamics (CFD) using the software Comsol Multiphysics 5.1.

Experimental

Materials

All the reagents were purchased from Sigma-Aldrich (Milan, IT) and SIAD (Bergamo, IT) and were of analytical grade. The solutions were prepared with deionized water. The following reagents were used: N_2, $NaBH_4$, $FeSO_4 \cdot 7H_2O$, and CMC (20,000 g/mol). The nanoparticles were produced in a four-baffled reactor.

The RT had a diameter $D_i = 0.33T$, where T (m) is the tank diameter, and a blade length and width of $D_i/4$ and $D_i/5$, respectively. The FPB turbine had a pitch angle of 45°, a diameter = D_i, and a blade length and width of $D_i/2$ and $D_i/5$, respectively.

The reactor temperature was kept constant at 25 °C using a thermostatic bath. The vessel was agitated using a Heidolph RZR 2020 with a controlled rotational velocity in the range 0–1500 rpm.

Please cite this article in press as: Vilardi, G., & Verdone, N. Production of metallic iron nanoparticles in a baffled stirred tank reactor: Optimization via computational fluid dynamics simulation. Particuology (2020), https://doi.org/10.1016/j.partic.2019.12.005

Methods

The produced nanoparticles were characterized via dynamic light scattering using a Zetasizer Nano ZS (Malvern, UK) to determine the PSD and zeta potential. The Fe(0) (%) production was determined quantitatively via the titration method reported elsewhere (Li, Ding, Wang, & Lei, 2016) and qualitatively via powder X-ray diffraction (XRD) using a Bruker D8 Advance. The nZVI solution viscosity was measured with a NDJ-1 viscometer equipped with column geometries of four scales numbered 1–4 and working in steady shear mode, and the pH was measured with a Crison 421 pH-meter.

The synthesis was carried out using reagent solutions prepared with deionized water previously de-oxygenated for 4 h at 50 °C under a nitrogen atmosphere.

Experimental procedure

The nZVI synthesis was performed according to a previous study (Vilardi, Di Palma, & Verdone, 2019), and the following operative parameters were varied: BH_4–/Fe(II) (mol/mol), iron initial concentration C_0 (mM), impeller geometry (RT or FPB), impeller clearance (C (cm)), and rotational velocity (N (rpm)). In brief, the CMC-Fe(II) solution was initially prepared through mechanical stirring (RT, N = 1000 rpm) under a nitrogen atmosphere until it reached complete dispersion, and subsequently the reducing solution of sodium borohydride was added with a peristaltic pump at a variable flowrate according to the blending mixing time calculated as reported below. The solution was stirred for 15 min after the reducing agent solution was added to allow complete formation of the nZVI:

$$2BH_4^- + Fe^{2+} + 6H_2O \rightarrow Fe(0) + 2B(OH)_3 + 7H_2. \quad (R1)$$

The black color indicating the beginning of particle production appeared immediately upon addition of the reducing agent, and the synthesis was conducted without a buffer.

In the first 14 runs, the Fe(0) (%) production was measured for each impeller using the following values for BH_4–/Fe(II): 2 (stoichiometric; see Eq. (R1)), 2.25, 2.5, 2.75, 3, 3.5, and 4, whereas the remaining parameters were kept constant (C_0 = 20 mM, C = 0.33T, and N = 1000 rpm). The ratio CMC/Fe(II) (mol/mol) was fixed at 0.005 according to a previous study (He & Zhao, 2007). Once the optimal BH_4–/Fe(II) ratio was determined, the other operative parameters were varied in the remaining 13 runs with the remaining parameters fixed to the following values: C_0 = 2, 20, and 200 mM; C = 0.15T, 0.25T, 0.33T, and 0.4T; and N = 250, 500, 750, 1000, 1250, and 1500 rpm. The set of optimal parameter values was determined according to the obtained PSD and zeta potential. After each run, the nZVI particles were immediately characterized through titration and with the zetasizer, and 10 mL of solution was vacuum filtered using NOVADEM PVDF membranes with 20 nm pores, dried, and stored under a nitrogen atmosphere for subsequent XRD analysis. The viscosity of the solution was measured only when C_0 was varied, to take into account the CMC concentration variation according to the fixed CMC/Fe(II) ratio. In addition, once all the optimal operative parameter values were found, kinetic experiments were conducted measuring the Fe(0) concentration during the nZVI synthesis at the following times: 10, 40, 60, 90, 120, 150, 180, 210, 240, 270, and 300 s. A different synthesis was performed for each time step (an additional 11 runs using the RT). Non-linear multiple regression of kinetic data was done with the *scipy.optimize.curve_fit* function of Python 3.6.1.

Each test was conducted in duplicate and the mean values were reported (the standard deviation was always <3.7%).

Data interpretation and CFD simulations

The obtained PSD and Fe(0) (%) production values were interpreted according to 3D simulations of the agitated vessel using Comsol Multiphysics. The two geometries are shown in Fig. 1(a) and (b) with C = 0.33T, indicating the addition of the reducing agent near the impeller.

The simulations were carried out with varying impeller clearance and solution viscosity due to varying CMC/Fe(II) as discussed previously. The optimal rotational velocity was fixed. The hydrodynamic behavior of a turbulent incompressible fluid is governed by the Navier–Stokes equations, which can be time-averaged to generate the Reynolds-averaged Navier–Stokes (RANS) equations for the velocity $\boldsymbol{u}$ (vector) and pressure p:

$$\frac{\partial \boldsymbol{u}}{\partial t} + \boldsymbol{u}\cdot\nabla\boldsymbol{u} + \nabla p = \nabla\cdot\left((\nu+\nu_T)\left[\nabla\boldsymbol{u} + \nabla\boldsymbol{u}^T\right]\right), \quad (1)$$

$$\nabla\cdot\boldsymbol{u} = 0, \quad (2)$$

where ν (m^2/s) is the kinematic viscosity of the fluid, and ν_T (m^2/s) is the turbulent eddy viscosity, which is supposed to contain the effect of unresolved velocity fluctuations. Additional relationships and hypotheses are necessary to close the RANS equations. In particular, the turbulence was modelled using a standard k–ε model whose transport equations are

$$\frac{\partial k}{\partial t} + \nabla\cdot\left(k\boldsymbol{u} - \frac{\nu_T}{\sigma_k}\nabla k\right) + \varepsilon = P_k, \quad (3)$$

$$\frac{\partial \varepsilon}{\partial t} + \nabla\cdot\left(\varepsilon\boldsymbol{u} - \frac{\nu_T}{\sigma_\varepsilon}\nabla\varepsilon\right) = \frac{\varepsilon}{k}(C_1P_k - C_2\varepsilon), \quad (4)$$

where $\nu_T = C_\mu k^2/\varepsilon$ is the turbulent viscosity, k (J/kg or m^2/s^2) the turbulent kinetic energy, ε (W/kg or m^2/s^3) the local turbulent energy dissipation rate, and P_k=$\nu_T/2\left[\nabla\boldsymbol{u} + \nabla\boldsymbol{u}^T\right]^2$. The last two terms represent dissipation and production of turbulent kinetic energy, respectively, and the default values of the above-reported empirical constants are set as: C_μ = 0.09, C_1 = 1.44, C_2 = 1.92, σ_k = 1.0, and σ_ε = 1.3. The system can be solved with proper initial and boundary conditions already implemented in the software code.

The power consumed by the impeller during stirring should be equal to the power dissipated by the liquid. Hence, the impeller power number (N_p) was calculated from volume integration of the turbulent energy dissipation rate predicted by the CFD model according to

$$N_{p,mod} = \frac{\int_0^{D_i/2}\int_0^H\int_0^{2\pi}\varepsilon r\rho_L dr dz d\theta}{N^3D_i^5\rho_L}, \quad (5)$$

where ρ_L (kg/m^3) is the liquid density, and (r, z, θ) are cylindrical coordinates. The simulations returned the values of ε and k, which were subsequently compared with those calculated from the correlations (Paul, Atiemo-Obeng, & Kresta, 2004)

$$k_{cal} = 0.06(N\pi D_i)^2, \quad (6)$$

$$\varepsilon_{cal} = 20\varepsilon_g = 20\frac{P}{V_T\rho_L} = 20\frac{N_P N^3 D_i^5}{V_T}, \quad (7)$$

where the product in brackets in Eq. (6) is the rotational velocity of the impeller tips; the subscript *cal* indicates that the parameter is calculated and not predicted by the CFD model; P (W) is the power required to drive the impeller and is given by $P = 2\pi N\gamma$, where γ (Nm) is the impeller torque; ε_g (m^2/s^3 or W/kg) is the turbulent kinetic energy dissipation rate with respect to the tank (usually one or two orders of magnitude lower than the value observed close to the impeller); and V_T (m^3) is the liquid volume in the tank. The $N_{p,mod}$ values were compared with the N_p values reported by other

Please cite this article in press as: Vilardi, G., & Verdone, N. Production of metallic iron nanoparticles in a baffled stirred tank reactor: Optimization via computational fluid dynamics simulation. *Particuology* (2020), https://doi.org/10.1016/j.partic.2019.12.005

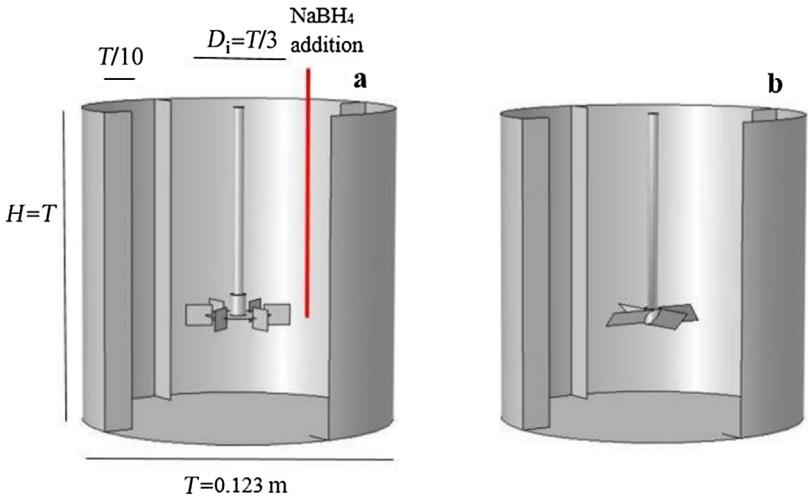

Fig. 1. Geometry of vessels equipped with Rushton turbine (a) and four-pitched blade (b) in Comsol Multiphysics environment.

authors for baffled turbulent agitated vessels equipped with a Rushton ($N_p = 5$, constant for $Re > 2000$) or four-pitched blade ($N_p = 0.87$, constant for $Re > 2000$) impeller (McCabe, Smith, & Harriott, 1993). These values are functions of the Reynolds number ($Re = ND_i^2/\nu$), the Froude number ($Fr = N^2 D_i/g$, where g (m/s^2) is the acceleration of gravity), and the geometry (T, H, C, etc.).

Finally, both the CFD-predicted and calculated ε and k values were used to calculate the blending time (τ_b) according to the Grenville theory (Eq. (8)) and the mixing time (τ_m) according to the Kolmogorov (τ_k), Batchelor (τ_{bc}), Corrsin (τ_c), and engulfment (τ_E) theories (Paul et al., 2004). The blending and mixing times were subsequently compared with the characteristic reaction time (τ_r) by calculating the mixing Damkohler number:

$$\tau_b = \begin{cases} \dfrac{5.4T^2}{NN_p^{0.33}D_i^2} & Re > 6400 \\ \dfrac{183^2T^2}{NReN_p^{0.66}D_i^2} & 500 < Re < 6400 \end{cases}, \quad (8)$$

$$\tau_k = \left(\frac{\upsilon}{\varepsilon}\right)^{0.5}, \quad (9)$$

$$\tau_{bc} = \frac{\lambda_b^2}{D}, \quad (10)$$

$$\tau_c = 2(0.39)^{0.66}\frac{k}{\varepsilon} + 0.5\tau_k \ln(Sc) \quad Sc \gg 1, \quad (11)$$

$$\tau_E = 17\tau_k, \quad (12)$$

$$\tau_r = \frac{2^{n-1}}{(n-1)k_{obs}C_0^{n-1}}, \quad (13)$$

$$Da_m = \frac{\tau_m}{\tau_r}, \quad (14)$$

where k_{obs} (L^{n-1}/mol^{n-1} s) is the kinetic constant of the nZVI synthesis reaction (of the pseudo-n^{th} order). To calculate the mixing Damkohler number, τ_m should be taken equal to τ_b if $\tau_r > \tau_b$ (kinetically controlled reaction), otherwise it should be taken equal to τ_m (mixed controlled reaction) (Paul et al., 2004). The bulk diffusion coefficient D of Fe(II) was taken to be 7.19×10^{-10} m^2/s according to Buffle, Zhang, and Startchev (2007).

The blending time for each configuration and operative condition was calculated and used to set the inlet flowrate of the reducing agent solution and to allow homogenization of the liquid bulk for each drop. In brief, the weight of a drop of water from the used tube (internal diameter of 8 mm) was measured as 0.08 g, corresponding to 0.08 mL, and the inlet flowrate Q_r (mL/min) was calculated as 0.08 mL/τ_b.

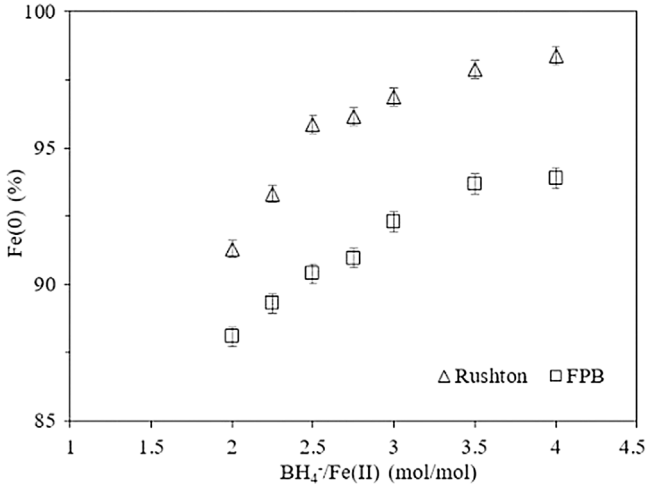

Fig. 2. nZVI production at different BH_4^-/Fe(II) molar ratios with varying impeller geometry ($C_0 = 20$ mM; temperature = 25 °C; $C = 0.33T$; $N = 1000$ rpm; $Q_r = 3$ and 2 mL/min for Rushton turbine and FPB impeller, respectively).

The mesh was composed of 461,600 volume elements, 16,374 surface elements, and 1164 boundary elements for the RT configuration and 240,706 volume elements, 13,358 surface elements, and 926 boundary elements for the FPB configuration. The impeller region (less than 1.5% of the tank volume) and regions near the vessel wall and baffle were meshed with more than 15% of the total grid used for the full tank to resolve the resulting steep gradients.

Results and discussion

nZVI production: effect of precursor/reducing agent molar ratio

Fig. 2 shows the Fe(0) (%) production with varying BH_4^-/Fe(II) molar ratio and impeller geometry, and Table 1 lists the calculated parameters of the first 14 runs.

As expected, the higher the reducing agent concentration, the higher the Fe(0) (%) production calculated as 100*Fe(0)/C_0. In particular, a notable Fe(0) (%) increase was observed when the BH_4^-/Fe(II) molar ratio was varied from 2.25 to 2.5 and the RT was used, reaching an Fe(0) (%) yield of about 96%. Similarly, Fe(0) (%) production increased to about 92.3% for the FPB when

Please cite this article in press as: Vilardi, G., & Verdone, N. Production of metallic iron nanoparticles in a baffled stirred tank reactor: Optimization via computational fluid dynamics simulation. *Particuology* (2020), https://doi.org/10.1016/j.partic.2019.12.005

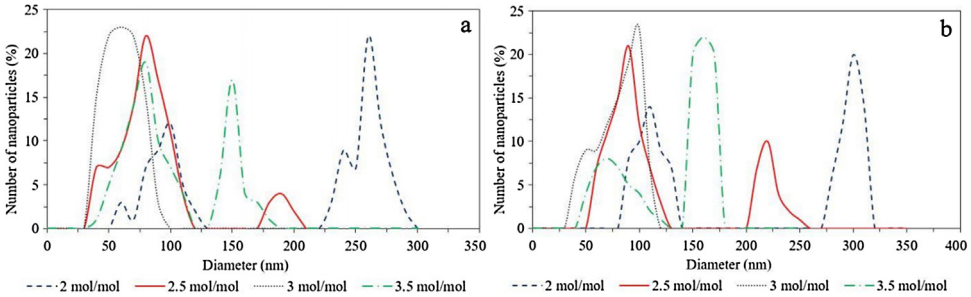

Fig. 3. PSD of nZVI at different BH_4–/Fe(II) molar ratios produced with Rushton (a) and FPB turbine (b).

Table 1
Calculated parameters of the first 14 runs.

Parameters	Value
ν (m^2/s)	2.17×10^{-6}
Re	12881.61
Sc	3.02×10^3
k_{cal} (J/kg)	0.277
τ_b Rushton (s)	1.72
τ_b FPB (s)	3.06
ε_{cal} Rushton (W/kg)	36.70
ε_{cal} FPB (W/kg)	6.39

Table 2
Calculated parameters of the six runs with BH_4–/Fe(II) molar ratio = 3.

	C_0 (mM)		
Parameters	2	20	200
ν (m^2/s)	1.7×10^{-6}	2.2×10^{-6}	3.8×10^{-5}
Re	16623.3	12881.6	747.1
Sc	2344.07	3024.95	52155.8
k_{cal} (J/kg)	0.277		
τ_b Rushton (s)	1.72	1.72	8.37
τ_b FPB (s)	3.06	3.06	26.54
ε_{cal} Rushton (W/kg)	36.70		
ε_{cal} FPB (W/kg)	6.39		

the BH_4–/Fe(II) molar ratio was varied from 2.75 to 3. However, the RT appeared more effective considering the higher Fe(0) (%) production obtained at fixed BH_4–/Fe(II). As reported by various authors, the RT is more effective for precipitating nanocrystals and nanoparticles than other impellers, because it notably reduces the induction time for the first nucleation. Thus, the RT is generally more recommended for chemical reactions than the FPB (Liu, Svärd, & Rasmuson, 2015; Tamburini et al., 2015). The blending time and kinetic energy dissipation rates of the two impellers were quite different. In fact, the RT had half the blending time of the FPB and a ε_{cal} value one order of magnitude larger. These results support the above-mentioned conclusions because a higher dissipation rate implies that more energy is transferred to the reactant liquid, which improves the reaction rate through a higher rate of molecular collisions (Laufhütte & Mersmann, 1987; Spalding, 1971). To select the optimal BH_4–/Fe(II) molar ratio, the PSDs of the runs with BH_4–/Fe(II) = 2.5, 3, and 3.5 were analyzed because the Fe(0) (%) increase for these tests was notable compared with that obtained with the stoichiometric value (Fig. 3).

The BH_4–/Fe(II) molar ratio strongly affected the nZVI PSD, which passed from a bimodal distribution at the stoichiometric ratio to an unimodal distribution when it was increased to 3. Therefore, 3 appears the optimal molar ratio for both impeller configurations. The mean size of the RT-produced nZVI particles was always lower than that of the FPB-produced ones, demonstrating the strong correlation among dissipated kinetic energy, reaction progress, and mean particle size. The mean particle sizes at the optimal molar ratio were 60.9 and 80.5 nm for the RT and FPB, respectively. Similar results were obtained by Hwang, Kim, and Shin (2011) and Turabik and Simsek (2017), who worked at lower rpms (400 and 250, respectively) and with other geometries, reporting an initial decrease in mean particle size as BH_4–/Fe(II) increased to a maximum and then an appreciable size increase as the molar ratio increased further. Hence, the above findings suggest fixing the optimal BH_4–/Fe(II) molar ratio at 3.

Effect of initial precursor concentration and viscosity

Once the BH_4–/Fe(II) molar ratio was fixed, the remaining runs were performed to determine the optimal initial precursor concentration (Fig. 4). Table 2 lists the calculated parameters for the six runs.

The increase in C_0 causes a viscosity increase owing to the higher CMC amount, leading to a decrease in *Re* and increase in *Sc*. Thus, the mixing flow in these conditions is in a transitional regime and no more in a turbulent one. This implies that the blending time should be raised to obtain the same homogeneity as in the runs with lower viscosities. Table 2 shows that the blending times of the runs with C_0 = 200 mM increased remarkably compared with the remaining runs, because the kinematic viscosity increased by one order of magnitude and *Re* decreased by the same order. This result agrees well with previous experiments using Rushton and pitched-blade turbines to blend liquids at increasing viscosity (Coyle, Hirschland, Michel, & Oldshue, 1970; Jones & Ozcan-Taskin, 2005). As expected, varying C_0 and viscosity has a negligible effect on Fe(0) (%) production or the XRD patterns. This is probably because the experiments used the optimal precursor/reducing agent molar ratio and calculated blending times. The XRD spectra clearly show the typical 45° peak of α-iron (Liu & Zhang, 2014). The characteristic peaks of iron oxide crystal (close to 63°) are also present, indicating that the particles were partially oxidized during sample preparation. As reported by various authors, a thin layer of iron oxides is necessary to prevent further oxidation of the product before its use (Crane & Scott, 2012; Fu, Dionysiou, & Liu, 2014; Joo, Feitz, Sedlak, & Waite, 2005; Keenan & Sedlak, 2008; Wang et al., 2016; Zhao et al., 2016).

In contrast to the findings on C_0–Fe(0) (%) correlation, the effect of C_0 on nZVI PSD was notable. As shown in Fig. 4(b) and (c), the PSD considerably varied with the initial amounts of the precursor and the corresponding reducing agent. An increase in C_0 produces an increase in mean nZVI size and formation of aggregates. This behavior has been observed by others (Hwang et al., 2011; Phenrat, Saleh, Sirk, Tilton, & Lowry, 2007) and might be explained by the increase in nZVI aggregation rate with nZVI concentration due to intensification of the magnetic force, notwithstanding the presence of more CMC (Phenrat et al., 2007). Another interesting result was that the average nZVI size increased at C_0 = 2 mM for both impellers. The higher amount of solvent molecules than produced nanoparticles and consequently lower CMC concentration probably improves oxidation of the produced nanoparticles, causing an increase in

Please cite this article in press as: Vilardi, G., & Verdone, N. Production of metallic iron nanoparticles in a baffled stirred tank reactor: Optimization via computational fluid dynamics simulation. *Particuology* (2020), https://doi.org/10.1016/j.partic.2019.12.005

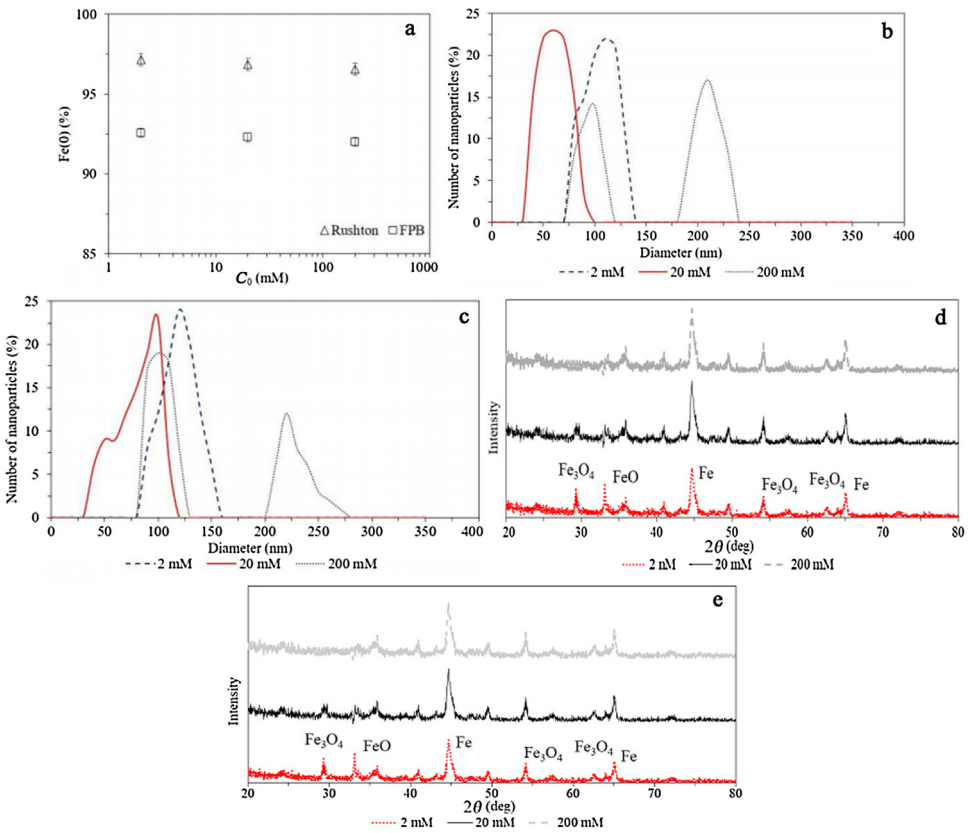

Fig. 4. Fe(0) (%) production (a), PSD for RT (b) and FPB (c), and XRD spectra for RT (d) and FPB (e) with different initial precursors (BH_4^-/Fe(II) = 3 mol/mol; temperature = 25 °C; $C = 0.33T$; $N = 1000$ rpm; $Q_r = 3$ and 2 mL/min when $C_0 = 2$ and 20 mM, respectively; $Q_r = 0.5$ and 0.25 mL/min for Rushton and FPB, respectively).

mean size and partial aggregation. Indeed, CMC not only reduces the aggregation tendency of nanoparticles, but decreases the diffusion coefficient of each chemical species in the bulk (including water molecules) via the viscosity increase (Tyrrell, 1981). Therefore, a decrease in CMC concentration and viscosity improves the partial oxidation and aggregation of suspended nanoparticles due to the water molecules (Keenan & Sedlak, 2008). This conclusion was also validated by the slight difference in XRD spectra of the nZVI produced with $C_0 = 2$ mM. In these cases, the iron oxide peaks are more evident than those of the other produced nZVI for both impellers. Finally, the zeta potentials were 27, 34, and 29 mV for the RT runs and 26.4, 34, and 28.1 mV for the FPB runs when C_0 was increased from 2 to 200 mM. The solution pH was in the range 6.2–6.9, in line with other reports (Sheng et al., 2016; Su & Kanjanawarut, 2009). The reported zeta potentials support the conclusions because the nanoparticles produced using the lowest and largest initial Fe(II) concentration were less stable than those produced when $C_0 = 20$ mM.

According to the above, C_0 was optimally fixed to 20 mM, and again the RT was more efficient than the FPB in producing nZVI with higher purity, unimodal size distribution, and smaller mean size.

Effects of impeller clearance and rotational velocity

Fig. 5 displays the results for nZVI production with varying impeller clearance.

The impeller clearance slightly affects Fe(0) (%) production independently of the impeller type. The production values were about constant with a modest increase or decrease at $C = 0.4T$ when the FPB or RT was used, respectively. This behavior has also been observed for the other parameters. A possible explanation is the very high reducing power of the $NaBH_4$ reagent: once the Fe(II)/BH_4^- stoichiometric ratio is exceeded and the optimal molar ratio with respect to the metal precursor has been reached, the fluid conditions and other parameters in the ranges we studied barely affect metal nanoparticle production.

In contrast, the impeller clearance had a notable effect on the PSD of the obtained nanoparticles. For the RT, decreasing C to $0.25T$ led to a reduction in mean nanoparticle size (50 nm). A further decrease to $0.15T$ caused a reduction in performance, because the distribution becomes bimodal and the peaks become larger. Studies on the effect of impeller clearance on mixing performance in stirred tank reactors have found that, when an RT is equipped, the decrease in clearance changes the two-loop flow typical of radial impellers to single-loop flow, reducing the mixing time (Ochieng, Onyango, Kumar, Kiriamiti, & Musonge, 2008). Indeed, decreasing C to $0.25T$ led also to a narrower distribution than those obtained with other C values. Different behavior is observed for the FPB. The resultant mean particle size is proportional to C, and the mean size decreases to 74 nm when C is fixed at $0.4T$. According to Svilović, Ćosić, Čelan, Bašić, and Kuzmanić (2018), the larger clearance of the FPB modifies the hydrodynamic field, improving the mixing conditions and leading to an increase in ε. A deeper discussion based on the CFD simulations is presented in Section "Effects of impeller clearance and rotational velocity".

Subsequently, the rotational impeller velocity was varied with the clearance fixed to $0.25T$ and $0.4T$ for the RT and FPB impeller, respectively. Fig. 6 shows the resultant Fe(0) (%) production and PSD for varying N and ε_{cal}, and Table 3 lists the blending times and Q_r values calculated for each run.

As expected, the rotational velocity increase supports the reaction, as evidenced by the almost linear Fe(0) (%)–N relationship, whereas Fe(0) (%) is proportional to $\ln(\varepsilon)$. The correlation coefficients of the regressed lines are all close to 0.98. An increase in N

Please cite this article in press as: Vilardi, G., & Verdone, N. Production of metallic iron nanoparticles in a baffled stirred tank reactor: Optimization via computational fluid dynamics simulation. *Particuology* (2020), https://doi.org/10.1016/j.partic.2019.12.005

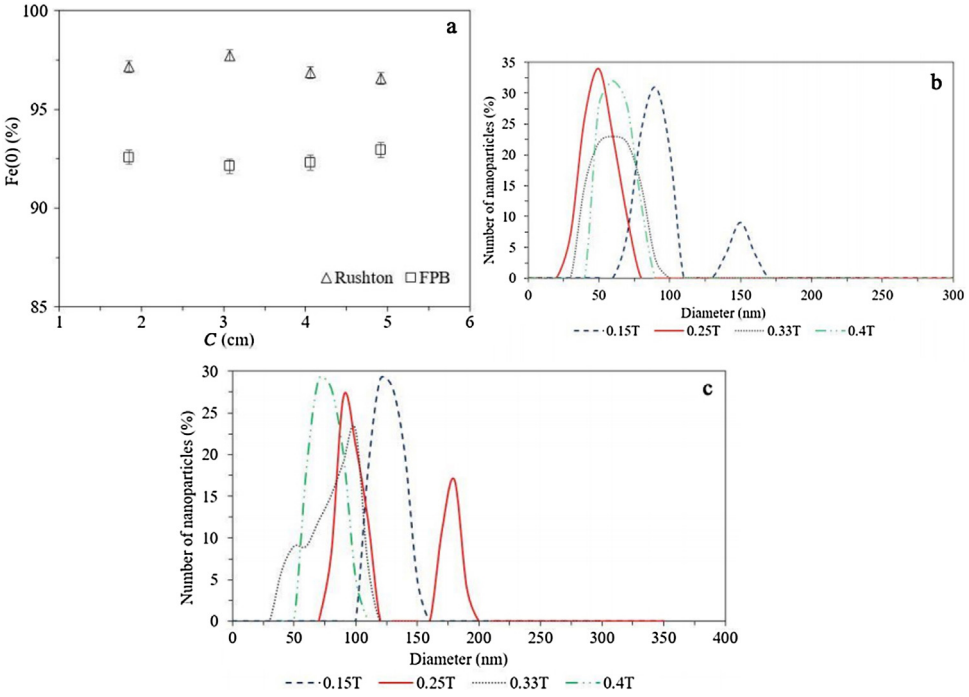

Fig. 5. Fe(0) (%) production (a) and PSD for RT (b) and FPB (c) with different impeller clearances (C_0 = 20 mM; BH_4–/Fe(II) = 3 mol/mol; temperature = 25 °C; N = 1000 rpm; Q_r = 3 and 2 mL/min for RT and FPB, respectively).

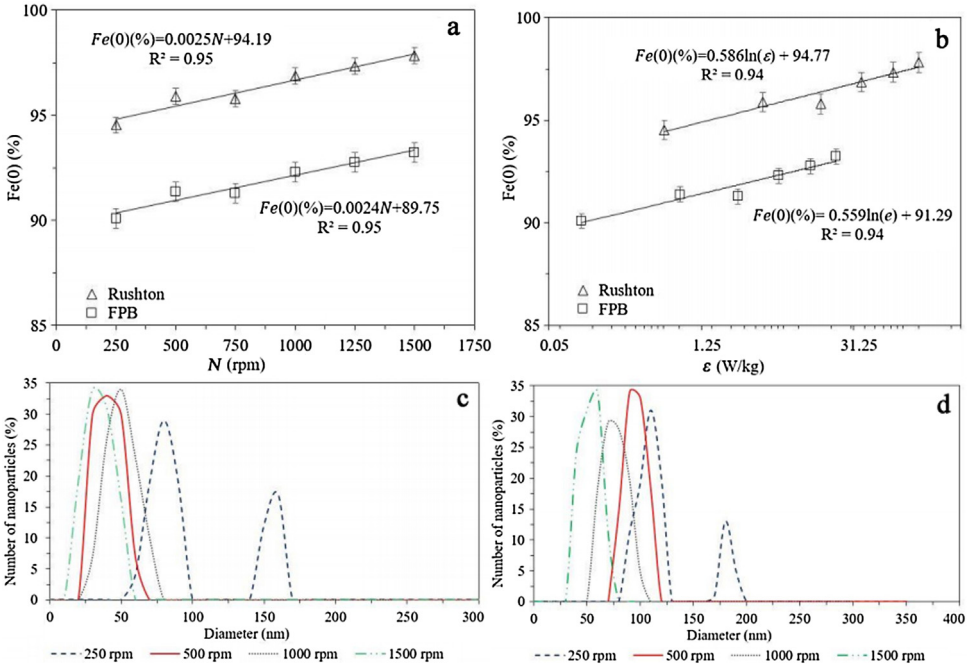

Fig. 6. Fe(0) (%) production vs. N (a) and vs. ε (b), and PSD for RT (c) and FPB (d) at different rotational velocities (C_0 = 20 mM; BH_4–/Fe(II) = 3 mol/mol; temperature = 25 °C; C = 0.25T and 0.4T for RT and FPB, respectively).

Table 3
Blending times and Q values for different N values.

	N (rpm)					
Parameters	250	500	750	1000	1250	1500
Q_r Rushton (mL/min)	0.14	1.40	2.10	2.80	3.50	4.20
Q_r FPB (mL/min)	0.05	0.79	1.18	1.57	1.97	2.36
Re	3220	6441	9661	12882	16102	19322
τ_b Rushton (s)	33.47	3.43	2.29	1.71	1.37	1.14
τ_b FPB (s)	106.14	6.11	4.07	3.05	2.44	2.04

leads to an increase in both turbulent kinetic energy and its dissipation rate, increasing the energy transferred by the mechanical stirrer to the mixed liquid as blending time decreases (Table 3). This increases the collision rates among the reagent molecules, favouring reaction progress (Laufhütte & Mersmann, 1987; Spalding, 1971; Temkin, 1977).

The rotational velocity has a considerable effect on the PSD of the produced nanoparticles (PSDs at 750 and 1250 rpm are not reported because they are almost equal to that obtained

Please cite this article in press as: Vilardi, G., & Verdone, N. Production of metallic iron nanoparticles in a baffled stirred tank reactor: Optimization via computational fluid dynamics simulation. *Particuology* (2020), https://doi.org/10.1016/j.partic.2019.12.005

at 1000 rpm). Independently from the used impeller, the mean nanoparticle size decreases as N increases from 250 to 500 rpm, increases as N increases further to 1000 rpm, and decreases again; the size reaches its minimum at $N = 1500$ rpm. Analogous trends were observed by Turabik and Simsek (2017), who used ferric chloride and hexadecyl-cetyl trimethyl ammonium bromide (HTAB) as the dispersing agent. While not specifying the reactor geometry or the impeller, they observed that when the stirring rates were varied (100, 400, 600, and 800 rpm), DLS results showed that the mean particle diameter changed (88.19, 13.25, 44.90, and 51.99 nm, respectively). Finally, the PSD became bimodal at 250 rpm, whereas it remained unimodal for the other N values. The minimum hydrodynamic diameter of the produced nZVI was 39.4 and 53.2 nm using the RT and FPB, respectively. Again, the RT demonstrated higher performance in nZVI production.

Accordingly, the rotational velocity was then fixed to 1500 rpm for the kinetic study and the CFD simulations.

Kinetic study

The mass transport equation of a reacting species in an ideal stirred tank reactor is

$$V_T \frac{d[Fe(0)]}{dt} = Q_{in}[Fe(0)]_0 - Q_{out}[Fe(0)]_{out} + rV_T, \quad (15)$$

where the subscripts "in" and "out" indicate the inlet and outlet flowrates, and the subscript 0 indicates the initial nZVI concentration, which is zero. For a batch system, Eq. (15) simplifies to

$$\frac{d[Fe(0)]}{dt} = r. \quad (16)$$

The reaction rate r (mol/m^3 s) depends on the supposed mechanism, reactant concentrations, mixing efficiency, temperature, and presence of other species in solution. Considering the reducing agent/precursor molar ratio to be larger than the stoichiometric one, a pseudo-n^{th}-order reaction mechanism was supposed:

$$r = -\frac{d[Fe(II)]}{dt} = k_{obs}[Fe(II)]^n. \quad (17)$$

Setting the initial condition ($t = 0$, $[Fe(II)] = C_0$) and rearranging Eq. (17) yields

$$[Fe(II)] = C_0\left(1 + C_0^{n-1}(n-1)k_{obs}t\right)^{\frac{1}{1-n}}. \quad (18)$$

Substituting this into Eq. (16) and then into Eq. (17) gives

$$\frac{d[Fe(0)]}{dt} = k_{obs}C_0{}^n\left(1 + C_0^{n-1}(n-1)k_{obs}t\right)^{\frac{n}{1-n}}. \quad (19)$$

Eq. (19) can be numerically solved using the initial condition ($t = 0$, $[Fe(0)] = 0$).

The model fit well to the experimental data (see Fig. 7), and the regressed value of the kinetic constant k_{obs} was found to be 0.018×10^4 L$^{3.1}$/(mol$^{3.1}$ s) with a regressed $n = 4.1$ (see Fig. 7). The objective function was 1.8×10^{-5}, and the correlation coefficients were both close to 0.99. From this, $t_r = 0.14$ s was calculated. This characteristic reaction time agrees with expectations because nanoparticle production is very fast. The data clearly show that the overall process finishes after about 75 s, after which an asymptotic trend is observed. The final Fe(0) (%) was close to 98% as obtained previously with optimal operating parameter values. The kinetic model was implemented in Comsol Multiphysics and coupled with the fluid dynamic interface. In particular, the model used was for a dilute transport species with reaction:

$$\frac{\partial c_j}{\partial t} = -u \cdot \nabla c_j - \nabla\left(-D_j \cdot \nabla c_j\right) + r_j, \quad (20)$$

where c (mol/m^3) is the specific chemical species concentration, and the subscript j indicates the specific chemical species. The

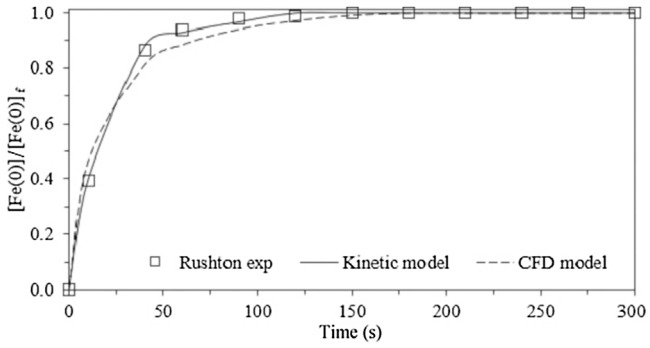

Fig. 7. Experimental data and kinetic model fitting of Fe(0) production using RT impeller ($N = 1500$ rpm; $C_0 = 20$ mM; BH_4–/Fe(II) = 3 mol/mol; temperature = 25 °C; $C = 0.25T$).

reaction term r is from the kinetic model of Eqs. (16)–(19). The time-dependent equations were solved by the CFD software, and the data fitting was performed using the Comsol optimizer, adopting as initial conditions the converged flow fields of the freeze-rotor simulations reported in section 2.4. The CFD model well fitted the experimental data, as shown in Fig. 7. Fig. 8 displays some time frames of the Fe(0) production according to the CFD model coupled with the dilute transport species with the reaction interface.

The CFD model well describes the production kinetics. At 30 s, the average Fe(0) molar concentration in the volume was about 12 mol/m^3, and at 60 s it rose to about 16 mol/m^3 to reach an asymptotic value of about 20 mol/m^3 after 150 s.

Computational fluid dynamics results and discussion

The results reported in previous sections were then interpreted analysing the flow patterns predicted by CFD simulations. Figs. 9–12 display the predicted velocity field ($\boldsymbol{u}$) and ε pattern with varying impeller clearance and type.

The CFD results for the RT velocity field show that the flow was less homogeneous at $C = 0.15T$ than at higher C. This is because the local velocity in the upper part of the reaction volume (immediately above the impeller) was lower than 1 m/s, whereas it was in the range 1–1.5 m/s in the remaining volume near the baffles. When $C > 0.25T$, the flow was more homogeneous and the local velocity in the reaction volume immediately above the impeller was higher than 1.5 m/s. As expected, the maximum $\boldsymbol{u}$ intensity was near the impeller, reaching a value of 3.5 m/s. The different established velocity fields in the two configurations, $C < 0.25T$ and $C > 0.25T$, are also well represented by the velocity vectors because their negligible variation in direction in the upper part of the reaction volume clearly shows the lower flow homogeneity in the former case than in the latter. Similar conclusions can be drawn for the FPB configuration, which shows a flow always less homogeneous than that of the RT with $\boldsymbol{u}$ intensities lower and not well distributed in the reaction volume. As expected, the maximum predicted ε values were near the impeller, where the energy dissipation was higher than that observed in the remaining volume. The overall energy dissipated in the RT was significantly higher than that dissipated with the FPB, as also shown by the maximum predicted ε in Table 4. The Fe(0) concentration field, expressed in terms of cross-sectional area in Figs. 12 and 13, clearly shows that the Fe(0) particles were produced near the impeller immediately after 30 s from addition of the reducing agent for both the RT and FPB. The impeller region is where ε was higher and where the local Fe(0) concentration almost reached 16 mM.

Tables 4 and 5 list the calculated and predicted torques, characteristic times, maximum ε values, and Damkohler mixing numbers.

Please cite this article in press as: Vilardi, G., & Verdone, N. Production of metallic iron nanoparticles in a baffled stirred tank reactor: Optimization via computational fluid dynamics simulation. *Particuology* (2020), https://doi.org/10.1016/j.partic.2019.12.005

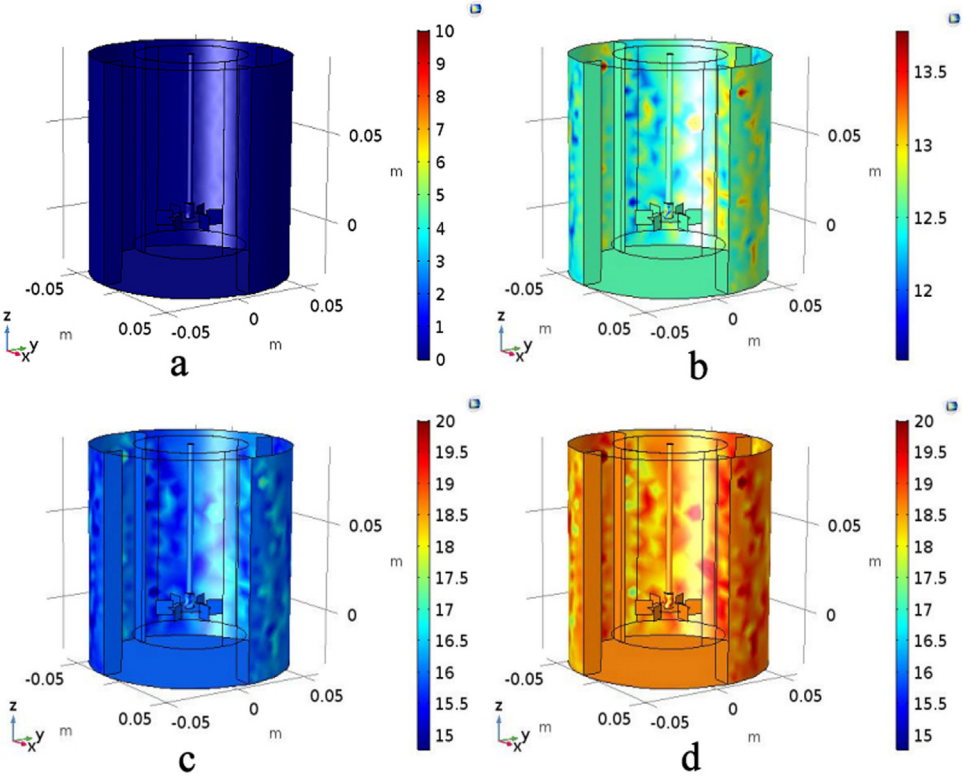

Fig. 8. Fe(0) concentration variation over time with Rushton turbine configuration at $t = 0$ s (a), $t = 30$ s (b), $t = 60$ s (c), and t=150 s (d) at $N = 1500$ rpm and $\nu = 2.2 \times 10^{-6}$ m^2/s.

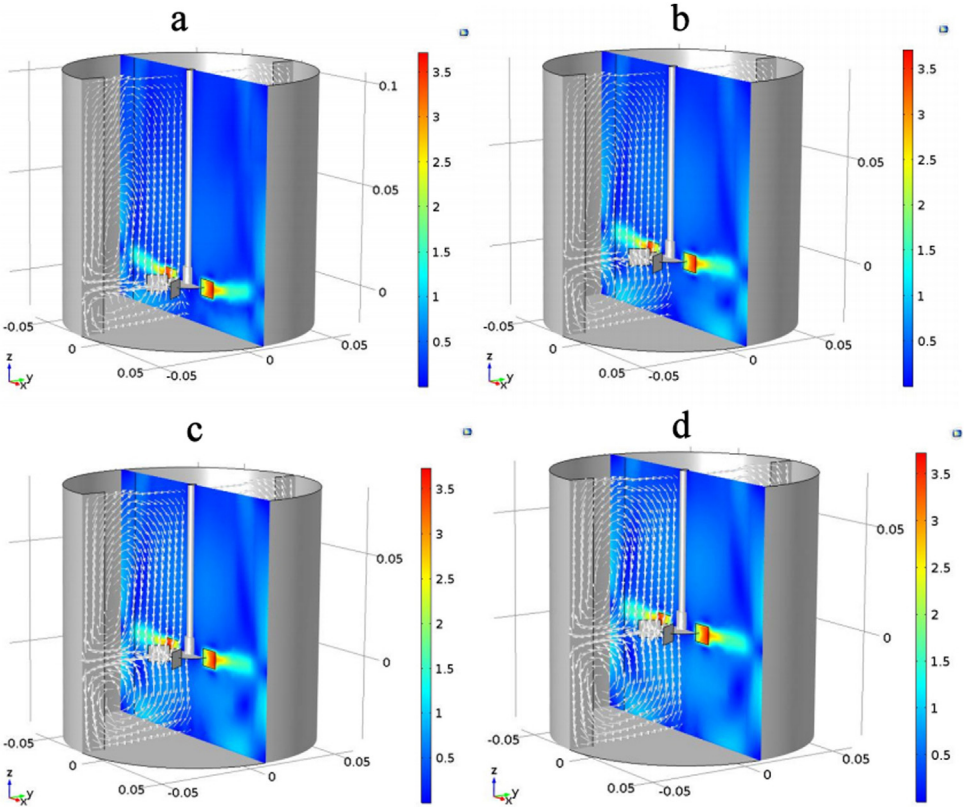

Fig. 9. Velocity field of Rushton turbine configuration at different C values: 0.15T (a), 0.25T (b), 0.33T (c), and 0.4T (d) at $N = 1500$ rpm and $\nu = 2.2 \times 10^{-6}$ m^2/s.

The power numbers predicted by the CFD model are similar to those in the literature; the predicted N_p for the RT is 4.6 instead of 5 and that of the FPB is 0.95 instead of 0.87. The results are similar for the predicted torques and blending times, which are less than 10% different from the calculations. As for the characteristic mixing times, the CFD predictions are all lower than the

Please cite this article in press as: Vilardi, G., & Verdone, N. Production of metallic iron nanoparticles in a baffled stirred tank reactor: Optimization via computational fluid dynamics simulation. *Particuology* (2020), https://doi.org/10.1016/j.partic.2019.12.005

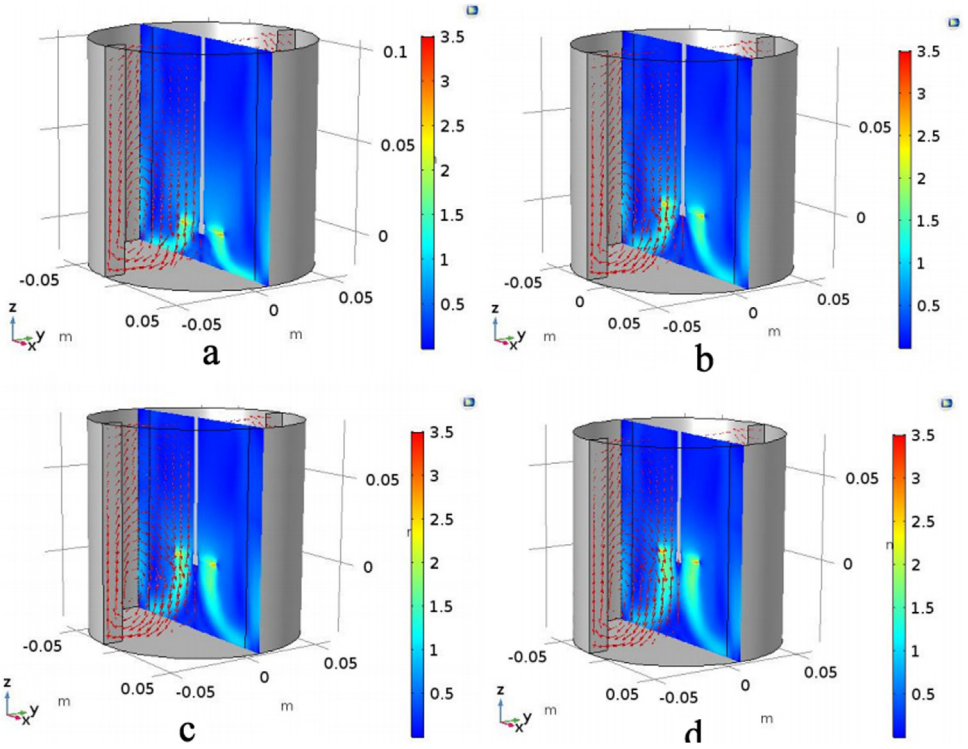

Fig. 10. Velocity field of FPB turbine configuration at different C values: 0.15T (a), 0.25T (b), 0.33T (c), and 0.4T (d) at N = 1500 rpm and $\nu = 2.2 \times 10^{-6}$ m^2/s.

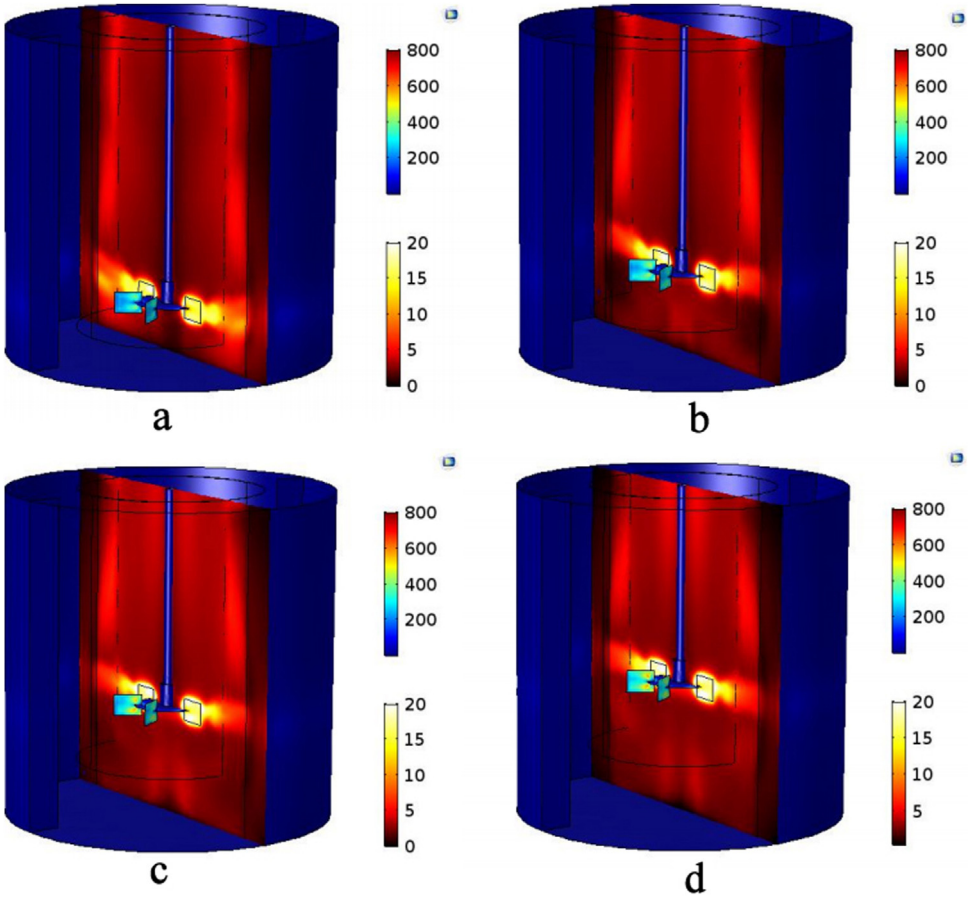

Fig. 11. ε pattern of Rushton turbine configuration at different C values: 0.15T (a), 0.25T (b), 0.33T (c), and 0.4T (d) at N = 1500 rpm and $\nu = 2.2 \times 10^{-6}$ m^2/s. The second legend is with respect to the Fe(0) concentration field after 30 s from the addition of the reducing agent, ranging from 0 to 20 mM.

Please cite this article in press as: Vilardi, G., & Verdone, N. Production of metallic iron nanoparticles in a baffled stirred tank reactor: Optimization via computational fluid dynamics simulation. *Particuology* (2020), https://doi.org/10.1016/j.partic.2019.12.005

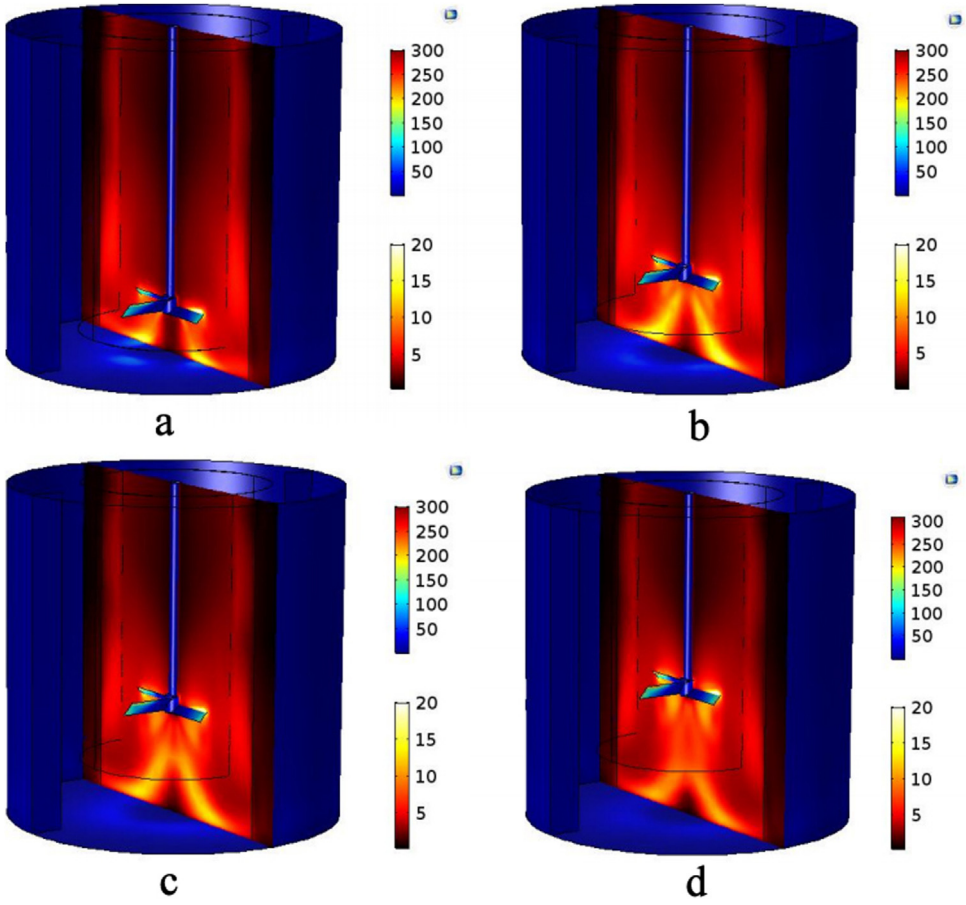

Fig. 12. ε pattern of FPB turbine configuration at different C values: 0.15T (a), 0.25T (b), 0.33T (c), and 0.4T (d) at N = 1500 rpm and $\nu = 2.2 \times 10^{-6}$ m^2/s. The second legend is with respect to the Fe(0) concentration field after 30 s from the addition of the reducing agent, ranging from 0 to 20 mM.

Table 4
CFD-predicted (mod) and calculated (cal) torques, blending times, and mixing times.

	Impeller	
Parameters	Rushton	FPB
N (rpm)	1500	
ν (m^2/s)	2.2×10^{-6}	
Re	19322	
N_p	5	0.87
$N_{p,mod}$	4.60	0.95
k_{cal} (J/kg)	0.622	
k_{max} (J/kg)	0.267	0.181
γ (Nm)	0.058	0.010
γ_{mod} (Nm)	0.053	0.011
τ_b (s)	1.14	2.04
$\tau_{b,mod}$ (s)	1.17	1.97
τ_k (s)	1.33×10^{-4}	3.18×10^{-4}
$\tau_{k,mod}$ (s)	5.53×10^{-5}	8.36E$\times 10^{-5}$
τ_{bc} (s)	1.33×10^{-4}	3.18×10^{-4}
$\tau_{bc,mod}$ (s)	5.53×10^{-5}	8.36×10^{-5}
τ_c (s)	5.93×10^{-3}	3.23×10^{-2}
$\tau_{c,mod}$ (s)	2.21×10^{-4}	3.35×10^{-4}
τ_E (s)	2.25×10^{-3}	5.40×10^{-3}
$\tau_{E,mod}$ (s)	9.40×10^{-4}	1.42×10^{-3}
η (m)	1.70×10^{-5}	2.63×10^{-5}
η_{mod} (m)	1.10×10^{-5}	1.35×10^{-5}
λ_b (m)	3.09×10^{-7}	4.78×10^{-7}
$\lambda_{b,mod}$ (m)	1.99×10^{-7}	2.45×10^{-7}
ε_{cal} (W/kg)	124	22
ε_{max} (W/kg)	712	311

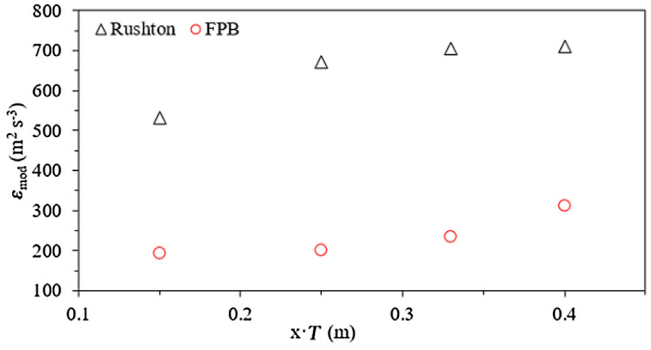

Fig. 13. ε_{mod}–C trend for the Rushton and FPB impellers (x is the multiplication factor for T, specifically 0.15, 0.25, 0.33, and 0.4).

Table 5
Predicted and calculated Damkohler mixing numbers.

	Damkohler mixing number			
	Rushton		FPB	
	CFD pred	cal	CFD pred	cal
Kolmogorov	3.95×10^{-4}	9.47×10^{-4}	5.97×10^{-4}	2.27×10^{-3}
Batchelor	3.95×10^{-4}	9.47×10^{-4}	5.97×10^{-4}	2.27×10^{-3}
Corrsin	1.58×10^{-3}	4.23×10^{-2}	2.39×10^{-3}	2.31×10^{-1}
Engulfment	6.71×10^{-3}	1.61×10^{-2}	1.02×10^{-2}	3.86×10^{-2}

calculated values, one order of magnitude in almost all cases. However, the predicted and calculated characteristic lengths are of the same order of magnitude. Finally, the calculated ε values are lower than those predicted by the model (the maximum values for C = 0.4T were considered). Consequently, the predicted Damkohler mixing numbers are lower than those calculated. The largest difference

Please cite this article in press as: Vilardi, G., & Verdone, N. Production of metallic iron nanoparticles in a baffled stirred tank reactor: Optimization via computational fluid dynamics simulation. *Particuology* (2020), https://doi.org/10.1016/j.partic.2019.12.005

is between the predicted and calculated FPB Corrsin mixing times (two orders of magnitude). The predicted value of ε in this case is one order of magnitude higher than the calculated one. The differences between the characteristic times derived from the different theories are in some cases remarkable, showing that the model should be selected considering the physical characteristics of the analyzed system. Because the characteristic dimension of the produced nanoparticles is in the range 10–100 nm, the Batchelor scale should be the more suitable for predicting the mixing characteristic time. However, as expected, the Damkohler mixing number was always lower than 1 independently of the theory selected, implying that the process is completely mixed controlled.

Regarding the predicted maximum ε at different C values, the trend observed for the RT configuration is significantly different from that for the FPB one. First, the RT, at fixed operating parameters and geometrical configuration, has higher energy dissipation than the FPB, which explains the enhanced nZVI production. Second, the maximum predicted ε in both cases increases with increasing C, but the two trends are substantially different, as Fig. 13 shows.

For the RT, ε_{mod} is 531 W/kg at $C = 0.15T$ and immediately increases to 671.14 W/kg at $C = 0.25T$, remaining about constant for higher C (up to 712 W/kg at $C = 0.4T$). In contrast, ε_{mod} for the FPB remarkably increases when C is higher than $0.33T$, rising from 234 W/kg to 311 W/kg at $C = 0.4T$. These different behaviors may explain the better nZVI production for the FPB when C is set to $0.4T$. Indeed, as experimentally observed by other authors (Chen, Wang, Guo, Wang, & Zheng, 2000; Siddiqui, Zhao, Kukukova, & Kresta, 2009), an increase in ε leads to a unimodal PSD and lower mean dimension. Regarding the different optimal C value obtained for the RT, C seems to affect nZVI production through a combination of both faster dissipation of turbulent kinetic energy and a different velocity field. In fact, the ε_{mod} values are quite similar when C is in the range $0.25T$–$0.33T$ but drop at $C = 0.15T$. This behavior may explain why the nZVI PSD becomes bimodal and the mean size tends to increase only when the clearance is reduced to $0.15T$. The velocity field offers the other explanation for the better performances at $C = 0.25T$. For an RT configuration, a decrease in the clearance may modify the classical two-loop flow typical of radial impellers to a single-loop flow and reduce the micromixing time, as reported elsewhere (Ochieng et al., 2008); this is not properly predicted by the CFD model. Therefore, even if the maximum ε_{mod} value is predicted at $C = 0.4T$, the combination of higher ε and lower micromixing time leads to the most efficient nZVI production, as experimentally observed.

Finally, Figs. 14 and 15 display the velocity fields ($\boldsymbol{u}$) and ε patterns at higher viscosity (3.75×10^{-5} m^2/s and $Re = 747.1$), obtained via the k–ε model.

The higher viscosity leads to a decrease in Re and turbulence of the system, simultaneously causing a decrease in turbulent energy dissipation rates predicted from the CFD model. The maximum ε values are 580.88 and 136.35 W/kg for the RT and FPB, respectively, significantly lower than the predicted values at fixed operating parameters and lower viscosity (704.2 and 234 W/kg for the RT and FPB, respectively). These results may explain the different performances observed in nZVI production, because, as already mentioned, the higher the energy dissipated in the agitated vessel, the lower the micromixing time and mean size of the produced nanoparticles (Chen et al., 2000; Siddiqui et al., 2009).

Reactor scale-up

The optimal operating parameter values obtained in previous sections made it possible to proceed with a scale-up of the technology. This is based on the mass balance equation for a continuous stirred tank reactor and the equality of impeller Reynolds numbers on the "small" (subscript s) and "big" (subscript b) scales:

$$V_T \frac{d[Fe(0)]}{dt} = Q_{in}[Fe(0)]_0 - Q_{out}[Fe(0)]_{out} + rV_T. \quad (21)$$

After we substitute Eq. (19) and set $Q = Q_{in} = Q_{out}$, $[Fe(0)]_0 = 0$, and steady-state conditions, Eq. (21) becomes

$$0 = -\frac{V_T}{Q}[Fe(0)]_{out} + k_{obs}C_0{}^n\left(1 + C_0^{n-1}(n-1)k_{obs}\frac{Q}{V_T}\right)^{\frac{n}{1-n}}. \quad (22)$$

This can be numerically solved to obtain the tank reactor volume.

Then, considering the liquid hold-up $H = T$, the tank diameter T can be determined for a cylindrical vessel as $T = (4V_T/\pi)^{1/3}$. These equations are coupled with that of a reactor scale-up based on fixed fluid-dynamic conditions (Paul et al., 2004):

$$(Re)_s = (Re)_b. \quad (23)$$

Using $D_i = T/3$ and considering the kinematic viscosity constant for simplicity results in

$$(N)_b = (N)_s\left[\frac{(T)_s}{(T)_b}\right]^2. \quad (24)$$

Fig. 16 displays a numerical example of T and N on the "big-scale" varying with respect to Q in the range 0.01–0.5 m^3/s (10–500 L/s).

The big-scale tank diameter increased from about 0.25 to 0.8 m for Q from 0.1 to 0.5 m^3/s, whereas the impeller rotational velocity decreased from about 7 to 0.4 rps (300–24 rpm). There are few published articles on the scale-up of metallic nanoparticle production, because this is one of the most difficult tasks owing to the reduced quality of product obtained on a larger scale ("the scale-up effect") (Shegokar, Singh, & Müller, 2011). Yin, Yamamoto, Wada, and Yanagida (2004) reported a microwave irradiation facility for producing silver nanoparticles. The synthesis was carried out using a microwave oven (650 W at 2.45 GHz) and 0.1 M trisodium citrate as a dispersing agent. The optimal production (98% of yield) was obtained using 1 min of microwave irradiation with a highly reducing agent and a formaldehyde/precursor (Ag^+) molar ratio of 15 mol/mol. However, the synthesis was in a 50 mL flask, and no scale-up procedure was discussed. In 2013, Tighe and co-authors discussed their experimental results on Ce–Zn nanoparticle synthesis using a supercritical water pilot-scale plant. The operative conditions were more severe than those in this work or other work in the literature (24.1 MPa and 450 °C). However, the results were promising, with a mean size of 1–5 nm and yield of 60%–99% depending on the mol% of Zn with respect to Ce (Tighe, Cabrera, Gruar, & Darr, 2013). Finally, a few recent studies have reported the possible scale-up of nanoparticle synthesis with microreactors. The scale-up in these studies is based on using a number of microreactors in parallel (Kockmann, Gottsponer, & Roberge, 2011; Rossetti & Compagnoni, 2016).

Conclusions

This study produced metallic iron nanoparticles in agitated vessels equipped with either a Rushton turbine or four-pitched blade impeller. The experimental results show that the Rushton impeller was more suitable for Fe(0) particle production, yielding a lower mean size than the FPB (39.4 instead of 53.2 nm) with unimodal size distribution and higher reaction conversions (about 98% instead of 94%). We investigated the effects on Fe(0) particle production of different operational parameters and system geometries. The optimal operating conditions found for nanoparticle production are: an impeller velocity of 1500 rpm, initial iron precursor concentration of 20 mM, molar ratio of reducing agent to iron precursor of

Please cite this article in press as: Vilardi, G., & Verdone, N. Production of metallic iron nanoparticles in a baffled stirred tank reactor: Optimization via computational fluid dynamics simulation. *Particuology* (2020), https://doi.org/10.1016/j.partic.2019.12.005

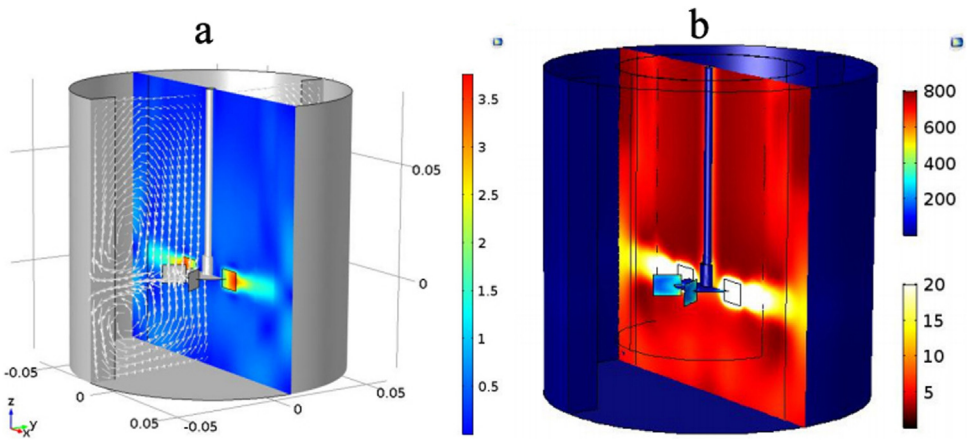

Fig. 14. Velocity field (a) and ε patterns (b) according to the k–ε model for the Rushton turbine configuration at $N = 1500$ rpm and $\nu = 3.75 \times 10^{-5}$ m^2/s.

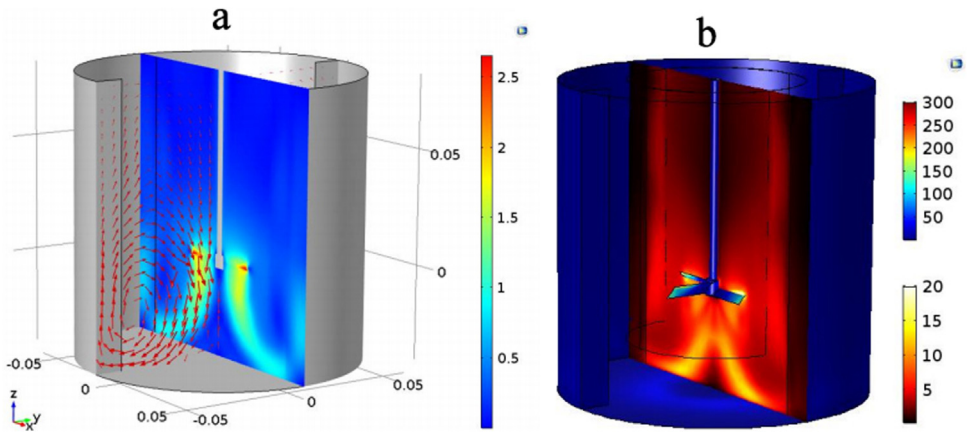

Fig. 15. Velocity field (a) and ε patterns (b) according to the k–ε model for the FPB impeller configuration at $N = 1500$ rpm and $\nu = 3.75 \times 10^{-5}$ m^2/s.

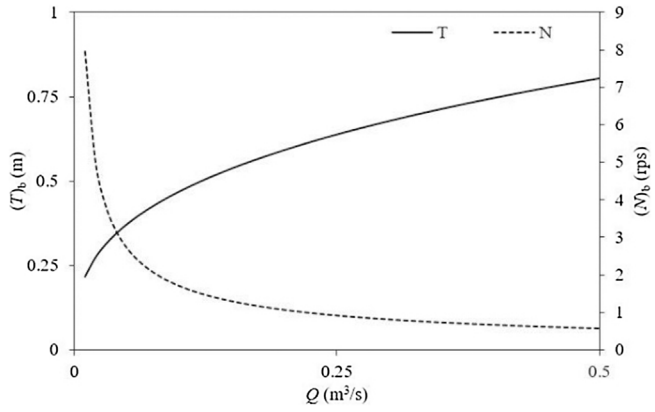

Fig. 16. Diameter and rotational velocity of the agitated vessel on the "big scale" as functions of Q ($C_0 = 0.2$ kmol/m^3; $(N)_s = 25$ rps; $(T)_s = 0.123$ m; $[Fe(0)]_0 = 0$ kmol/m^3; $[Fe(0)]_{out} = 0.19$ kmol/m^3).

3 mol/mol, and impeller clearance of 0.25 and 0.4 times the vessel diameter for Rushton and four-pitched blade impellers, respectively. In contrast to the results for the nZVI mean dimension and particle size distribution, Fe(0) (%) was less affected by the operating parameters in the ranges observed.

The observed reaction kinetics is very fast. The experimental data were successfully fitted to a pseudo-nth-order kinetic model, returning a reaction order $n = 4.1$ and a regressed kinetic constant equal to 0.018×10^4 L$^{3.1}$/(mol$^{3.1}$ s), from which a characteristic reaction time of 0.14 s was calculated. CFD well predicts the powers of the two configurations. The predicted maximum k and ε values are of the same order of magnitude as those calculated from theoretical correlations, except for the FPB. In this case, the calculated ε was one order of magnitude lower than the predicted value. However, the CFD results and predictions agree with expectations, and the obtained mixing Damkohler numbers clearly show that the production process was mixed controlled.

Declaration of interests

The authors declare that they have no known competing financial interests or personal relationships that could have appeared to influence the work reported in this paper.

References

Afify, A. A., & Elgazery, N. S. (2016). Effect of a chemical reaction on magnetohydrodynamic boundary layer flow of a Maxwell fluid over a stretching sheet with nanoparticles. *Particuology*, *29*, 154–161.

Batchelor, G. K. (1959). Small-scale variation of convected quantities like temperature in turbulent fluid Part 1. General discussion and the case of small conductivity. *Journal of Fluid Mechanics*, *5*(01), 113–133.

Buffle, J., Zhang, Z., & Startchev, K. (2007). Metal flux and dynamic speciation at (bio) interfaces. Part I: Critical evaluation and compilation of physicochemical parameters for complexes with simple ligands and fulvic/humic substances. *Environmental Science and Technology*, *41*(22), 7609–7620.

Chen, J. F., Wang, Y. H., Guo, F., Wang, X. M., & Zheng, C. (2000). Synthesis of nanoparticles with novel technology: High-gravity reactive precipitation. *Industrial & Engineering Chemistry Research*, *39*, 948–954.

Coyle, C. K., Hirschland, H. E., Michel, B. J., & Oldshue, J. Y. (1970). Mixing in viscous liquids. *AIChE Journal*, *16*(6), 903–906.

Please cite this article in press as: Vilardi, G., & Verdone, N. Production of metallic iron nanoparticles in a baffled stirred tank reactor: Optimization via computational fluid dynamics simulation. *Particuology* (2020), https://doi.org/10.1016/j.partic.2019.12.005

Crane, R. A., & Scott, T. B. (2012). Nanoscale zero-valent iron: Future prospects for an emerging water treatment technology. *Journal of Hazardous Materials*, *211–212*, 112–125.
Di Palma, L., Gueye, M. T., & Petrucci, E. (2015). Hexavalent chromium reduction in contaminated soil: A comparison between ferrous sulphate and nanoscale zero-valent iron. *Journal of Hazardous Materials*, *281*, 70–76.
Farrell, D., Majetich, S. A., & Wilcoxon, J. P. (2003). Preparation and characterization of monodisperse Fe nanoparticles. *The Journal of Physical Chemistry B*, *107*(40), 11022–11030.
Fu, F., Dionysiou, D. D., & Liu, H. (2014). The use of zero-valent iron for groundwater remediation and wastewater treatment: A review. *Journal of Hazardous Materials*, *267*, 194–205.
Gavi, E., Marchisio, D. L., & Barresi, A. A. (2008). On the importance of mixing for the production of nanoparticles. *Journal of Dispersion Science and Technology*, *29*(4), 548–554.
Halperin, W. P. (1986). Quantum size effects in metal particles. *Reviews of Modern Physics*, *58*(3), 533–606.
He, F., & Zhao, D. (2007). Manipulating the size and dispersibility of zerovalent iron nanoparticles by use of carboxymethyl cellulose stabilizers. *Environmental Science & Technology*, *41*(17), 6216–6221.
Huber, D. L. (2005). Synthesis, properties, and applications of iron nanoparticles. *Small*, *1*(5), 482–501.
Hwang, Y.-H., Kim, D.-G., & Shin, H.-S. (2011). Effects of synthesis conditions on the characteristics and reactivity of nano scale zero valent iron. *Applied Catalysis B: Environmental*, *105*(1–2), 144–150.
Jones, P. N., & Ozcan-Taskin, G. N. (2005). Effects of physical property differences on blending. *Chemical Engineering & Technology*, *28*(8), 908–914.
Joo, S. H., Feitz, A. J., Sedlak, D. L., & Waite, T. D. (2005). Quantification of the oxidizing capacity of nanoparticulate zero-valent iron. *Environmental Science & Technology*, *39*(5), 1263–1268.
Keenan, C. R., & Sedlak, D. L. (2008). Factors affecting the yield of oxidants from the reaction of nanoparticulate zero-valent iron and oxygen. *Environmental Science & Technology*, *42*(4), 1262–1267.
Kockmann, N., Gottsponer, M., & Roberge, D. M. (2011). Scale-up concept of single-channel microreactors from process development to industrial production. *Chemical Engineering Journal*, *167*(2–3), 718–726.
Laufhütte, H. D., & Mersmann, A. (1987). Local energy dissipation in agitated turbulent fluids and its significance for the design of stirring equipment. *Chemical Engineering & Technology*, *10*(1), 56–63.
Li, L., Fan, M., Brown, R. C., Van Leeuwen, J., Wang, J., Wang, W., et al. (2006). Synthesis, properties, and environmental applications of nanoscale iron-based materials: A review. *Critical Reviews in Environmental Science and Technology*, *36*(5), 405–431.
Li, S., Ding, Y., Wang, W., & Lei, H. (2016). A facile method for determining the Fe(0) content and reactivity of zero valent iron. *Analytical Methods*, *8*(6), 1239–1248.
Li, Y., Hu, Y., Huang, G., & Li, C. (2013). Metallic iron nanoparticles: Flame synthesis, characterization and magnetic properties. *Particuology*, *11*(4), 460–467.
Liu, J., Svärd, M., & Rasmuson, Å. C. (2015). Influence of agitation on primary nucleation in stirred tank crystallizers. *Crystal Growth & Design*, *15*(9), 4177–4184.
Liu, A., & Zhang, W.-X. (2014). Fine structural features of nanoscale zero-valent iron characterized by spherical aberration corrected scanning transmission electron microscopy (Cs-STEM). *Analyst*, *139*, 4512–4518.
Mata, R., Bhaskaran, A., & Sadras, S. R. (2016). Green-synthesized gold nanoparticles from Plumeria alba flower extract to augment catalytic degradation of organic dyes and inhibit bacterial growth. *Particuology*, *24*, 78–86.
McCabe, W. L., Smith, J. C., & Harriott, P. (1993). *Unit operations of chemical engineering*. New York: McGraw-Hill.
Mohammed, L., Gomaa, H., Ragab, D., & Zhu, J. (2017). Magnetic nanoparticles for environmental and biomedical applications: A review. *Particuology*, *30*, 1–14.
Ochieng, A., Onyango, M. S., Kumar, A., Kiriamiti, K., & Musonge, P. (2008). Mixing in a tank stirred by a Rushton turbine at a low clearance. *Chemical Engineering and Processing: Process Intensification*, *47*(5), 842–851. http://dx.doi.org/10.1016/J.CEP.2007.01.034
Paul, E. L., Atiemo-Obeng, V. A., & Kresta, S. M. (2004). *Handbook of industrial mixing: Science and practice*. New York: Wiley-Interscience.
Phenrat, T., Saleh, N., Sirk, K., Tilton, R. D., & Lowry, G. V. (2007). Aggregation and sedimentation of aqueous nanoscale zerovalent iron dispersions. *Environmental Science & Technology*, *41*(1), 284–290.
Pohl, B., Jamshidi, R., Brenner, G., & Peuker, U. A. (2012). Experimental study of continuous ultrasonic reactors for mixing and precipitation of nanoparticles. *Chemical Engineering Science*, *69*(1), 365–372.
Pope, S. B. (2000). *Turbulent flows*. Cambridge: Cambridge University Press.
Richardson, L. F. (1922). *Weather prediction by numerical process*. Cambridge: Cambridge University Press.
Rossetti, I., & Compagnoni, M. (2016). Chemical reaction engineering, process design and scale-up issues at the frontier of synthesis: Flow chemistry. *Chemical Engineering Journal*, *296*, 56–70.
Shegokar, R., Singh, K. K., & Müller, R. H. (2011). Production stability of stavudine solid lipid nanoparticles—From lab to industrial scale. *International Journal of Pharmaceutics*, *416*(2), 461–470.
Sheng, G., Alsaedi, A., Shammakh, W., Monaquel, S., Sheng, J., Wang, X., et al. (2016). Enhanced sequestration of selenite in water by nanoscale zero valent iron immobilization on carbon nanotubes by a combined batch, XPS and XAFS investigation. *Carbon*, *99*, 123–130.
Shi, L. N., Lin, Y. M., Zhang, X., & Chen, Z. L. (2011). Synthesis, characterization and kinetics of bentonite supported nZVI for the removal of Cr(VI) from aqueous solution. *Chemical Engineering Journal*, *171*(2), 612–617.
Siddiqui, M. K. J., Zhao, Y., Kukukova, A., & Kresta, S. M. (2009). Characteristics of a confined impinging jet reactor: Energy dissipation, homogeneous and heterogeneous reaction products, and effect of unequal flow. *Industrial & Engineering Chemistry Research*, *48*, 7945–7958.
Singh, R., Misra, V., & Singh, R. P. (2011). Synthesis, characterization and role of zero-valent iron nanoparticle in removal of hexavalent chromium from chromium-spiked soil. *Journal of Nanoparticle Research*, *13*(9), 4063–4073.
Spalding, D. B. (1971). Mixing and chemical reaction in steady confined turbulent flames. *Symposium (International) on Combustion*, *13*(1), 649–657.
Su, X., & Kanjanawarut, R. (2009). Control of metal nanoparticles aggregation and dispersion by PNA and PNA/DNA complexes, and its application for colorimetric DNA detection. *ACS Nano*, *3*(9), 2751–2759.
Surinwong, S., & Rujiwatra, A. (2013). Ultrasonic cavitation assisted solvothermal synthesis of superparamagnetic zinc ferrite nanoparticles. *Particuology*, *11*(5), 588–593.
Svilović, S., Ćosić, M., Čelan, A., Bašić, A., & Kuzmanić, N. (2018). Influence of axial impeller off-bottom clearance on copper exchange kinetics on zeolite NaX in batch reactor. In *ISCRE 25 - Bridging Science&technology*, *154* (pp. 546–547).
Tamburini, A., Cipollina, A., Grisafi, F., Scargiali, F., Micale, G., & Brucato, A. (2015). Comparison of agitators performance for particle suspension in top-covered unbaffled vessels. *Chemical Engineering Transactions*, *43*, 1585–1590.
Temkin, M. I. (1977). Transfer of dissolved matter between a turbulently moving. *Kinetica i Kataliz*, *18*, 493–496.
Tighe, C. J., Cabrera, R. Q., Gruar, R. I., & Darr, J. A. (2013). Scale up production of nanoparticles: Continuous supercritical water synthesis of Ce–Zn oxides. *Industrial & Engineering Chemistry Research*, *52*(16), 5522–5528.
Turabik, M., & Simsek, U. B. (2017). Effect of synthesis parameters on the particle size of the zero valent iron particles. *Inorganic and Nano-Metal Chemistry*, *47*(7), 1033–1043.
Tyrrell, H. J. V. (1981). Diffusion and viscosity in the liquid phase. *Science Progress (1933-)*, *67*(266), 271–293.
Vilardi, G., Di Palma, L., & Verdone, N. (2019). A physical-based interpretation of mechanism and kinetics of Cr(VI) reduction in aqueous solution by zero-valent iron nanoparticles. *Chemosphere*, *220*, 590–599.
Vispute, T. P., Zhang, H., Sanna, A., Xiao, R., & Huber, G. W. (2010). Renewable chemical commodity feedstocks from integrated catalytic processing of pyrolysis oils. *Science*, *330*(6008), 1222–1227.
Wang, L., & Fox, R. O. (2004). Comparison of micromixing models for CFD simulation of nanoparticle formation. *AIChE Journal*, *50*(9), 2217–2232.
Wang, X., Cong, S., Wang, P., Ma, J., Liu, H., & Ning, P. (2017). Novel green micelles Pluronic F-127 coating performance on nano zero-valent iron: Enhanced reactivity and innovative kinetics. *Separation and Purification Technology*, *174*, 174–182.
Wang, X., Le, L., Wang, A., Liu, H., Ma, J., & Li, M. (2016). Comparative study on properties, mechanisms of anionic dispersant modified nano zero-valent iron for removal of Cr(VI). *Journal of the Taiwan Institute of Chemical Engineers*, *66*, 115–125.
Xin, J., Tang, F., Zheng, X., Shao, H., & Kolditz, O. (2016). Transport and retention of xanthan gum-stabilized microscale zero-valent iron particles in saturated porous media. *Water Research*, *88*, 199–206.
Xu, R. (2008). Progress in nanoparticles characterization: Sizing and zeta potential measurement. *Particuology*, *6*(2), 112–115.
Yin, H., Yamamoto, T., Wada, Y., & Yanagida, S. (2004). Large-scale and size-controlled synthesis of silver nanoparticles under microwave irradiation. *Materials Chemistry and Physics*, *83*(1), 66–70.
Zhao, X., Liu, W., Cai, Z., Han, B., Qian, T., & Zhao, D. (2016). An overview of preparation and applications of stabilized zero-valent iron nanoparticles for soil and groundwater remediation. *Water Research*, *100*, 245–266.

Please cite this article in press as: Vilardi, G., & Verdone, N. Production of metallic iron nanoparticles in a baffled stirred tank reactor: Optimization via computational fluid dynamics simulation. *Particuology* (2020), https://doi.org/10.1016/j.partic.2019.12.005